Nanotechnology Perceptions
ISSN 1660-6795
www.nano-*ntp.com*

Mn-Doped Molecularly Imprinted Hollow Tio_2 Nanospheres for Selective Visible-Light Photocatalytic Degradation of Enrofloxacin

Simrat Kaur, Kuldeep Kaur*

Department of Chemistry, Mata Gujri College, Fatehgarh Sahib-140406, Punjab, India
**Corresponding Author: shergillkk@gmail.com*
Received: 09 January, 2020
Accepted: 01 April, 2020
https://doi.org/10.62441/nano-ntp.v14i3.

The increasing occurrence of fluoroquinolone antibiotics in aquatic systems poses significant environmental risks due to their persistence and role in antimicrobial resistance. Herein, Mn-doped molecularly imprinted hollow TiO_2 nanospheres (HC@Mn–MIP–TiO_2) were synthesized via a template-assisted sol–gel method using enrofloxacin as the imprint molecule. The integration of Mn doping, molecular imprinting, and hollow architecture enhanced visible-light absorption, selective adsorption, and photocatalytic activity. Characterization confirmed the formation of hollow anatase TiO_2 with uniform Mn incorporation and a reduced band gap (~2.78 eV). The imprinted photocatalyst exhibited high adsorption capacity (149.2 mg g^{-1}) and selective recognition toward enrofloxacin. Under visible light, HC@Mn–MIP–TiO_2 achieved ~99.9% degradation within 90 min with superior kinetics compared to the non-imprinted analogue. The catalyst also showed excellent stability and maintained >97% degradation efficiency in real water matrices, highlighting its potential for selective antibiotic removal from contaminated waters.

Keywords: Molecular imprinting; Mn-doped TiO_2; Hollow nanospheres; Enrofloxacin; Visible-light photocatalysis; Antibiotic removal.

1. Introduction

The extensive use of antibiotics in human medicine, veterinary practice, and agriculture has led to their widespread release into aquatic environments, contributing to the global spread of antimicrobial resistance (AMR) [1]. These compounds enter natural waters through pharmaceutical effluents, hospital and domestic wastewater, and agricultural runoff [2], promoting the proliferation of resistant microorganisms even in ecosystems without direct antibiotic exposure [3]. Fluoroquinolones such as enrofloxacin are of particular concern due to their high stability, poor biodegradability, and frequent detection in surface waters. Even at low concentrations, they can disrupt microbial ecosystems and facilitate the spread of resistance genes, creating significant environmental and public health risks. Therefore, efficient methods for removing such contaminants from water are urgently needed.

Semiconductor photocatalysis using TiO_2 is a promising approach for degrading persistent organic pollutants because of its chemical stability, non-toxicity, and ability to generate reactive oxygen species. However, pristine TiO_2 exhibits limited visible-light activity due to its wide band gap (~3.2 eV), rapid electron–hole recombination, and poor selectivity toward

specific contaminants. Transition-metal doping has been widely explored to address these limitations. Incorporation of manganese (Mn) into the TiO_2 lattice introduces impurity states within the band gap, enabling enhanced visible-light absorption and improved charge carrier separation [4-7]. Consequently, Mn-modified TiO_2 has shown enhanced photocatalytic activity compared with pristine TiO_2 [8-10]. Selectivity toward target pollutants can be improved through molecular imprinting technology. In this approach, template molecules are incorporated during synthesis and subsequently removed to generate recognition cavities complementary to the target analyte [11-13]. These imprinted sites promote selective adsorption and facilitate subsequent photocatalytic degradation [14]. Molecular imprinting has been successfully applied for the selective removal of various environmental pollutants, including dyes, pesticides, and pharmaceuticals [15-16]. Structural engineering through hollow nanostructures represents another effective strategy to enhance photocatalytic performance. Hollow nanospheres provide high surface area, improved mass transfer, and enhanced light utilization, often resulting in superior photocatalytic efficiency compared with solid materials [17-18]. Template-assisted sol–gel methods using silica nanospheres are particularly effective for synthesizing hollow TiO_2 structures with controlled morphology [19-20].

Although Mn doping, molecular imprinting, and hollow structuring have individually been explored to improve TiO_2 photocatalysis, their combined integration for selective enrofloxacin degradation has received limited attention. In this study, Mn-doped molecularly imprinted hollow TiO_2 nanospheres (HC@Mn–MIP–TiO_2) were synthesized by integrating these three strategies. SiO_2 nanospheres served as sacrificial templates to create hollow structures, Mn doping enhanced visible-light activation, and enrofloxacin acted as the imprint molecule to generate selective recognition sites. The synthesized materials were characterized using TEM, SEM, FTIR, XRD, and UV–Vis diffuse reflectance spectroscopy, and their adsorption and photocatalytic performances toward enrofloxacin degradation were systematically evaluated.

2. Materials and Methods

2.1 Chemicals and Reagents

Titanium(IV) isopropoxide (TTIP, ≥97%) and tetraethyl orthosilicate (TEOS, ≥98%) were used as precursors for TiO_2 and SiO_2 nanospheres, respectively. Manganese(II) nitrate tetrahydrate ($Mn(NO_3)_2{\cdot}4H_2O$, ≥98%) served as the Mn dopant source. Enrofloxacin (analytical grade) was used as the template molecule and target pollutant, while ciprofloxacin was used as a structural analogue for selectivity studies. Ammonium hydroxide (25–30%) was used as a catalyst for the Stöber synthesis of silica spheres, and Triton X-100 acted as a surfactant during shell formation. Sodium hydroxide (NaOH, ≥98%) was used for alkaline etching and template removal. Ethanol, methanol, and isopropanol were used as solvents during synthesis and washing steps. Hydrochloric acid and sodium hydroxide were used for pH adjustment. Deionized water (≥18 MΩ·cm) was used throughout all experiments. All chemicals were of analytical grade sourced from Sigma-Aldrich and used without further purification.

2.2 Synthesis of Mn-Doped Molecularly Imprinted Hollow TiO_2 Nanospheres

2.2.1 Synthesis of silica cores (SiO_2 nanospheres)

Uniform SiO_2 nanospheres were synthesized using a modified Stöber method. A mixture of isopropanol (20 mL), deionized water (4 mL), and ammonia solution (30%, 1 mL) was stirred at 500 rpm for 10 min at 25 °C. TEOS (1 mL) was then added dropwise and the reaction mixture was stirred at room temperature for 2 h. The resulting suspension was centrifuged (6000 rpm, 5 min), washed three times with ethanol, and stored in ethanol for further use.

2.2.2 Synthesis of Mn-doped molecularly imprinted TiO_2 shell on silica cores (SiO_2@Mn–MIP-TiO_2)

To coat silica nanospheres with Mn-doped molecularly imprinted TiO_2, 0.25 g of SiO_2 nanospheres were dispersed in 20 mL ethanol by sonication (30 min). Ethanol (20 mL), deionized water (0.5 mL), and Triton X-100 (2 mL) were added and the mixture was stirred overnight at 25 °C (600 rpm) to stabilize the cores. Separately, TTIP (1.5 mL) was dissolved in 40 mL ethanol, while $Mn(NO_3)_2 \cdot 4H_2O$ (12.7 mg, 1 mol% Mn:Ti) and enrofloxacin (18 mg) were dissolved in minimal DI water and ethanol–methanol (9:1), respectively. The Mn and ENR solutions were added to the TTIP solution under stirring (800 rpm), and the resulting precursor mixture was introduced dropwise into the SiO_2 dispersion at 25 °C. The reaction was stirred for 2 h to form a Mn-doped TiO_2 shell, followed by aging overnight. The obtained SiO_2@Mn–MIP–TiO_2 composite was centrifuged (6000 rpm, 5 min), washed with ethanol and DI water, and air-dried at 40 °C.

2.2.3 Removal of silica core and enrofloxacin template

The silica core and enrofloxacin template were removed by alkaline etching. The Mn-doped core–shell nanospheres were treated with 2.5 M NaOH (pH ≈ 13.6) under stirring for 24 h, with the solution replaced every 4 h. The resulting particles were centrifuged (6000 rpm, 6–8 min), washed with deionized water until neutral pH, followed by ethanol washing to obtain hollow Mn-doped molecularly imprinted TiO_2 (HC@Mn–MIP–TiO_2). The product was vacuum-dried at 40 °C for 12 h and calcined at 300 °C for 2 h. The synthesis scheme is illustrated in Fig. 1. A non-imprinted control (HC@Mn–NIP–TiO_2) was prepared similarly without the template molecule.

Figure 1: Graphical Representation

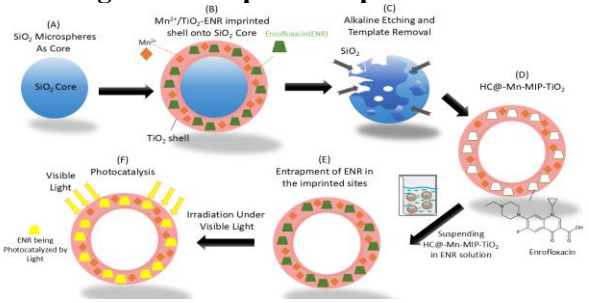

3. Results and Discussion

3.1 Structural and Phase Analysis (XRD)

The crystal structure and phase composition of HC@Mn–MIP–TiO_2 were examined by X-ray diffraction (XRD) (Fig. 2). The diffraction peaks at $2\theta \approx 25.3°$ (101), 37.8° (004), 48.0° (200), 53.9° (105), 55.1° (211), 62.7° (204), 68.8° (116), and 70.3° (220) correspond to the anatase phase of TiO_2 (JCPDS No. 21-1272). No peaks related to rutile, brookite, or manganese oxide phases were observed, indicating that the anatase structure was preserved after Mn doping, molecular imprinting, alkaline etching, and calcination.

The absence of secondary phases suggests that Mn species are either highly dispersed or incorporated into the TiO_2 lattice below the XRD detection limit. The average crystallite size, calculated from the anatase (101) peak using the Scherrer equation, was approximately 66 nm, confirming the nanocrystalline nature of the material. Peak broadening is attributed to small crystallite size and lattice distortion resulting from Mn incorporation and hollow structuring.

Figure 2: XRD of HC@Mn-MIP-TiO_2

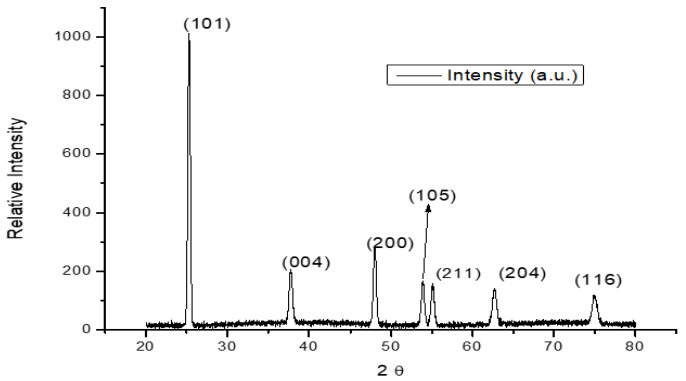

3.2 Doping confirmation/DRS

The undoped samples exhibit an absorption edge at ~385–390 nm, corresponding to the characteristic band-gap transition of anatase TiO_2 (~3.2–3.3 eV). After Mn doping, the absorption edge shifts toward longer wavelengths, extending to ~445 nm for HC@Mn–MIP–TiO_2, indicating enhanced visible-light absorption compared to the undoped sample (Fig. 3). UV–Vis diffuse reflectance spectra for HC@Mn–MIP–TiO_2 and HC@Undoped–MIP–TiO_2 are shown in Fig. 4 and 5.

Figure 3: UV-Vis Diffuse Reflectance Spectra Showing Absorption Edge Shift

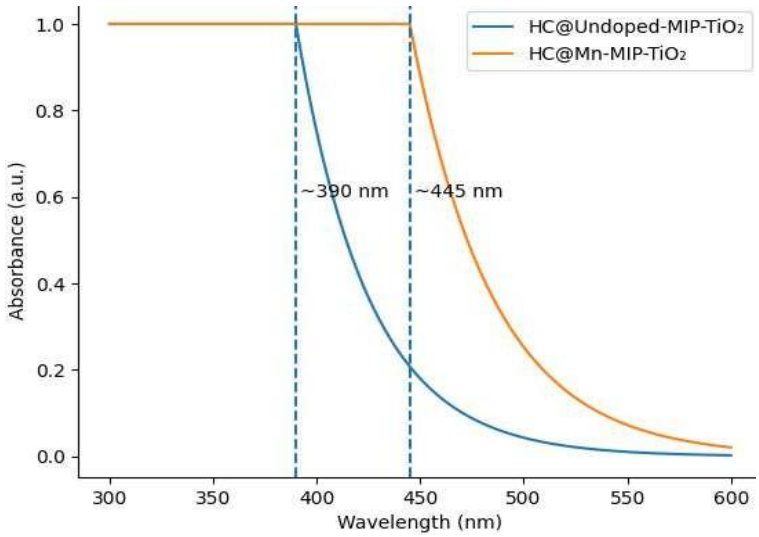

Tauc analysis further confirms this shift, revealing a band-gap reduction from 3.30 eV for HC@Undoped–MIP–TiO_2 to 2.78 eV for HC@Mn–MIP–TiO_2. This band-gap narrowing is attributed to the introduction of impurity energy levels by Mn dopants, which extend light absorption into the visible region.

3.3 Template removal and functional groups (FT-IR)

The FTIR spectra of the Mn-doped molecularly imprinted photocatalyst (HC@Mn–MIP–TiO_2) and its non-imprinted counterpart (HC@Mn–NIP–TiO_2) are shown in Fig. 6. Pure enrofloxacin exhibits characteristic bands at 1715–1720 cm^{-1} (C=O stretching) and 1240–1280 cm^{-1} (C–F stretching), which disappear after template removal, confirming successful extraction of enrofloxacin from the imprinted cavities. Both HC@Mn–MIP–TiO_2 and HC@Mn–NIP–TiO_2 display a broad band around 3400 cm^{-1} attributed to O–H stretching of surface hydroxyl groups and a band near 1630–1640 cm^{-1} corresponding to adsorbed water.

Figure 4: Tauc plot for HC@Undoped-MIP-TiO_2, showing a direct optical band gap of ~3.3 eV

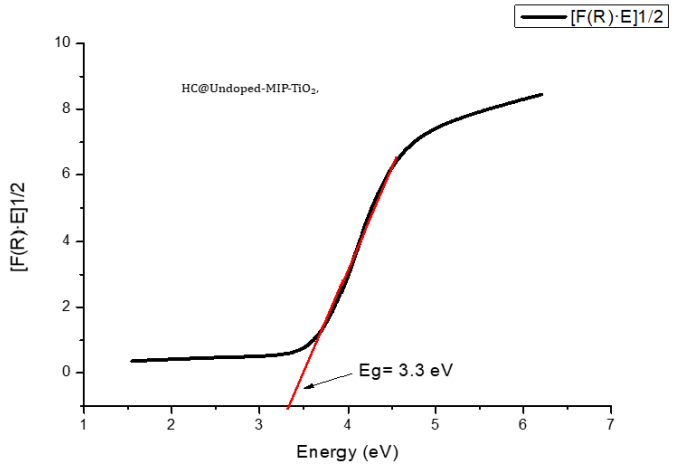

Figure 5: Tauc plot HC@Mn-MIP-TiO_2, showing a direct band-gap energy of ~2.78 eV

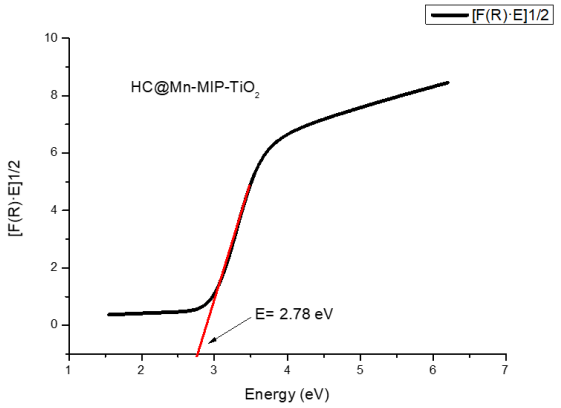

The low-frequency region (700–500 cm^{-1}) shows characteristic Ti–O–Ti lattice vibrations of anatase TiO_2. The broadening and slight shift of the Ti–O band (~500–650 cm^{-1}) suggest lattice distortion caused by Mn incorporation (Ti–O–Mn/Mn–O interactions). These spectral features confirm successful incorporation of enrofloxacin during synthesis and its subsequent removal to generate imprinted cavities. The disappearance of template-related bands (C=O at 1715–1720 cm^{-1} and C–F at 1240–1280 cm^{-1}) further verifies effective template extraction, while the broad O–H band around 3400 cm^{-1} indicates abundant surface hydroxyl groups favorable for adsorption and photocatalytic reactions.

Figure 6: FTIR spectra of Mn-doped molecularly imprinted TiO_2 nanospheres before (HC@Mn-MIP-TiO_2-WT) and after (HC@Mn-MIP-TiO_2) template removal

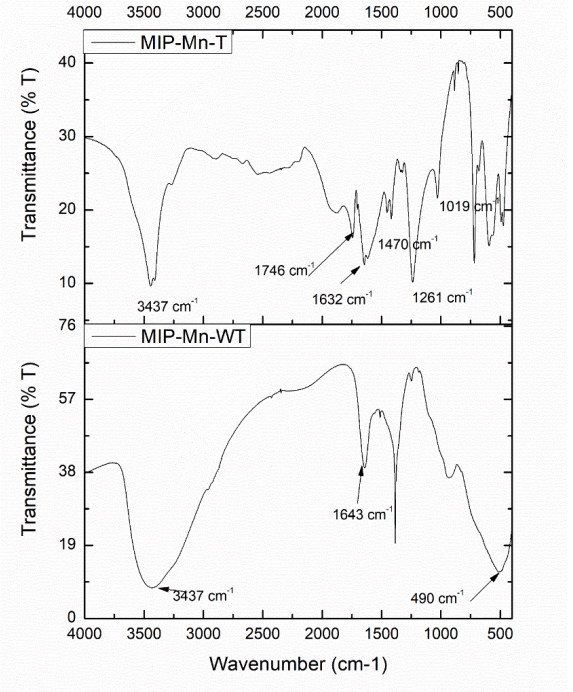

3.4 SEM/EDS

3.4.1 SEM

Scanning electron microscopy (SEM) was used to investigate the surface morphology of the Mn-doped molecularly imprinted hollow TiO_2 nanospheres (HC@Mn–MIP–TiO_2) (Fig. 7). The SEM images reveal aggregated spherical structures composed of nanoscale primary particles, forming a rough and highly textured surface.

Figure 7: SEM Images of HC@Mn-TiO_2 (a)-(c) at 500 nm and (d) at 1 mm

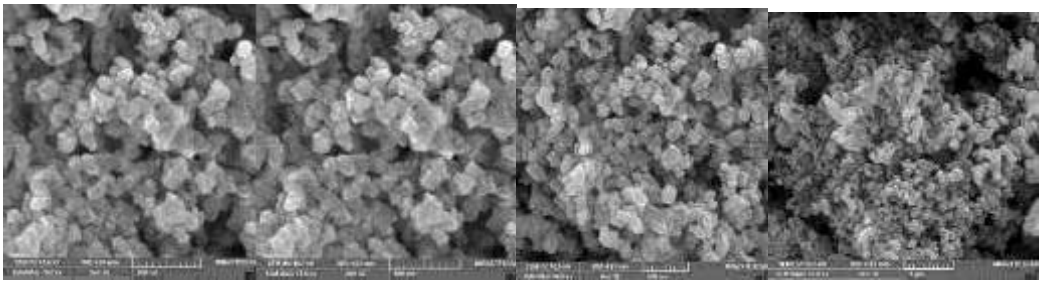

(a) (b) (c) (d)

At ~10,000× magnification (scale bar 1 μm), the nanospheres appear uniformly distributed without structural collapse, indicating that the sol–gel coating, alkaline etching, and calcination processes preserved the morphology. The rough surface and interparticle voids enhance surface area, facilitate mass transfer of enrofloxacin molecules, and improve light scattering within the hollow structure. The absence of distinct crystalline facets, large segregated domains, or structural cracks suggests homogeneous TiO_2 shell formation and good mechanical stability after silica core removal.

3.4.2 EDS Elemental Composition and Doping Confirmation

Energy-dispersive X-ray spectroscopy (EDS) coupled with SEM was used to analyze the elemental composition and verify Mn doping in HC@Mn–MIP–TiO_2 nanospheres. The EDS spectra display characteristic peaks of Ti, O, and Mn, confirming successful incorporation of manganese into the TiO_2 matrix (Fig. 8).

Figure 8: EDS of HC@Mn-MIP-TiO_2

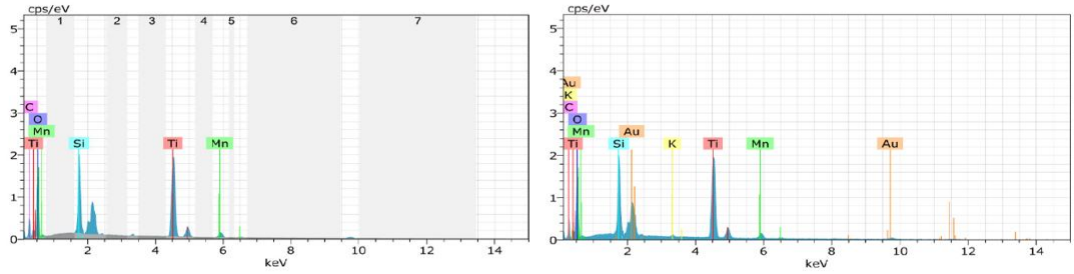

Quantitative EDS analysis shows manganese content of ~3.9–4.0 wt.% (≈1.6–2.0 at.%), confirming low-level Mn incorporation in the TiO_2 matrix (Table 1).

Table 1: EDS quantitative analysis

Element	Series	Unnormalized C (wt.%)	Normalized C (wt.%)	Atomic C (at.%)	Error (3σ, wt.%)
Titanium	K-series	24.65	38.34	18.07	2.24
Manganese	K-series	2.53	3.93	1.62	0.34
Oxygen	K-series	24.11	37.49	52.88	9.65
Silicon	K-series	6.32	9.83	7.90	0.88
Carbon	K-series	6.68	10.40	19.53	3.24

Element	Series	Unnormalized C (wt.%)	Normalized C (wt.%)	Atomic C (at.%)	Error (3σ, wt.%)
Total		64.29	100.00	100.00	

Oxygen is the dominant element (≈52–53 at.%), followed by titanium (≈18–22 at.%), consistent with a TiO_2-rich composition, noting the limitations of EDS for light-element analysis. Silicon (~8–10 wt.%) indicates residual silicon species within the interaction volume but at levels much lower than intact silica cores. Carbon originates from carbon tape or surface contamination, while trace potassium and gold arise from precursor residues and the conductive coating used during SEM analysis.

3.4.3 Elemental Mapping and Spatial Distribution

Elemental mapping further reveals the spatial distribution of elements within the HC@Mn–MIP–TiO_2 nanospheres.

Figure 9: Elemental Mapping (a)-(d) of Ti, Mn, O and Si

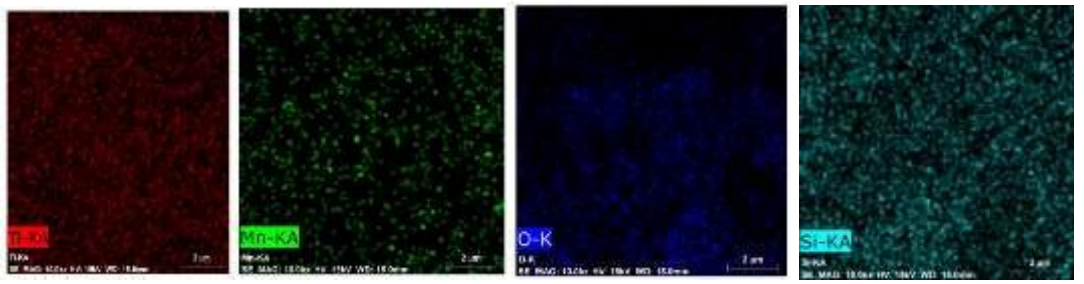

(a) (b) (c) (d)

The Ti-Kα and O-K maps show uniform and overlapping distributions, confirming the formation of a continuous TiO_2 shell (Fig. 9). The Mn-Kα map indicates homogeneous dispersion of Mn throughout the nanospheres without clustering or phase segregation, which is beneficial for effective charge separation. Weak and diffuse Si-Kα signals suggest near-complete removal of the silica core, confirming the successful formation of hollow structures rather than residual core–shell particles.

3.5 TEM analysis

TEM micrographs of HC@Mn–MIP–TiO_2 obtained at moderate (~58,000×) and high (~1.05 M×) magnifications reveal particles with a distinct core–shell architecture (Fig. 10). A clear contrast between the lighter interior and darker outer shell indicates the presence of electron-transparent hollow cores surrounded by electron-dense TiO_2 shells, confirming the formation of hollow structures. The hollow interiors are centrally located and continuous, while the shell thickness remains relatively uniform across particles, suggesting controlled shell growth rather

than structural collapse. These features are consistent with hollow TiO_2 nanostructures typically obtained through sacrificial-template sol–gel methods.

Figure 10: TEM Images of HC@Mn-MIP-TiO_2 at various magnifications a) 1.05 Mx b) 74000 x c) 120 kx d) A single Sphere

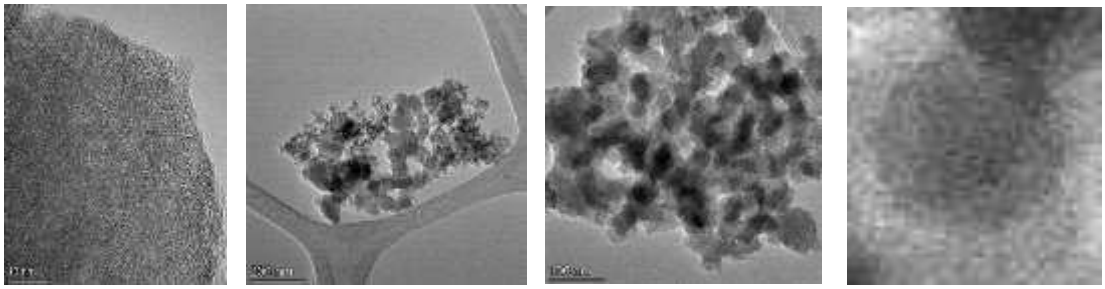

(a) (b) (c) (d)

TEM analysis confirms the successful formation of a hollow-core morphology in HC@Mn–MIP–TiO_2, where a well-defined TiO_2 shell surrounds an electron-transparent interior. The shell appears dense and nanostructured with a thickness of ~66–100 nm (estimated using ImageJ) and shows no cracks or discontinuities, indicating that template removal and imprinting did not compromise structural integrity. At lower magnification, the particles appear as loosely aggregated hollow spheres, typical of TiO_2 nanomaterials due to surface hydroxyl interactions, while individual shell boundaries remain clearly distinguishable. High-resolution TEM images display clear lattice fringes within the shell, confirming the crystalline nature of the TiO_2 framework and suggesting nanocrystalline anatase domains, consistent with XRD results. No secondary nanoparticles or Mn-rich clusters are observed, indicating that Mn is either incorporated into the TiO_2 lattice or highly dispersed at the atomic level. This uniform distribution, supported by EDS analysis, confirms homogeneous Mn incorporation within the TiO_2 shell rather than the formation of separate manganese oxide phases.

4. Adsorption performance and selectivity

4.1 Effect of pH on enrofloxacin adsorption

The effect of solution pH on the adsorption of enrofloxacin (ENR) onto HC@Mn–MIP–TiO_2 was investigated in the pH range 4–10 using an initial ENR concentration of 5 ppm. The pH was adjusted using dilute HCl or NaOH without buffering to avoid competition with adsorption sites, and remained stable within ±0.2 units during the experiments. As shown in Fig. 11, adsorption capacity strongly depended on pH due to the pH-dependent speciation of ENR and the surface properties of TiO_2.

At acidic pH (<6), adsorption was relatively low because ENR predominantly exists in its cationic form and experiences electrostatic repulsion from positively charged TiO_2 surfaces. Adsorption increased significantly near neutral pH, reaching a maximum at pH 6.5–7.0, where ENR mainly exists in a zwitterionic form ($pKa_1 \approx 6.2$; $pKa_2 \approx 8.8$), enabling favorable interactions with imprinted sites. At alkaline pH (>8), adsorption decreased due to the

formation of anionic ENR species and increased electrostatic repulsion from negatively charged TiO_2 surfaces. Based on these results, pH ~7.0 was selected as the optimum condition for subsequent adsorption and isotherm studies.

Figure 11: Effect of pH on the adsorption of ENR by HC@Mn-MIP-TiO_2

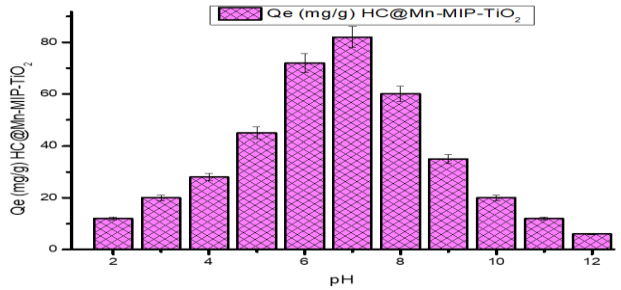

4.2 Adsorption Kinetics and Equilibrium Time

The adsorption kinetics of enrofloxacin (ENR) onto HC@Mn–MIP–TiO_2 were studied by monitoring residual ENR concentration over 5–120 min at pH ~7.0 and 25 ± 1 °C. As shown in Fig. 12, adsorption was rapid initially, with significant ENR uptake within the first 30 min. The rate gradually decreased and approached equilibrium within 60–90 min, as indicated by stabilization of the solution concentration. No significant increase in adsorption occurred beyond 90 min; however, an equilibration time of 120 min was used for isotherm studies to ensure complete equilibrium. The relatively fast equilibrium suggests efficient mass transfer and good accessibility of imprinted binding sites in the hollow Mn-doped TiO_2 nanospheres.

Figure 12: Adsorption Kinetics of ENR on HC@Mn-MIP-TiO_2

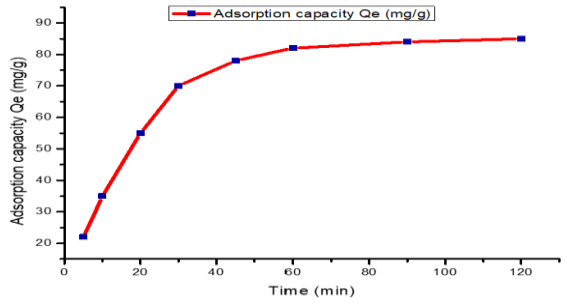

4.3 Adsorption Isotherms

The equilibrium adsorption behavior of enrofloxacin (ENR) on HC@Mn–MIP–TiO_2 and HC@Mn–NIP–TiO_2 was investigated over an initial ENR concentration range of 0.5–10 ppm at pH ~7.0 and 25 °C (Fig. 13). For both materials, the adsorption capacity (q_e) increased with

increasing equilibrium concentration (C_e), indicating a concentration-dependent process. However, HC@Mn–MIP–TiO_2 exhibited significantly higher adsorption capacity than HC@Mn–NIP–TiO_2 across the entire concentration range.

At low concentrations, HC@Mn–MIP–TiO_2 showed a sharp increase in q_e, reflecting the presence of high-affinity imprinted binding sites that preferentially capture ENR molecules. In contrast, HC@Mn–NIP–TiO_2 displayed a more gradual adsorption increase due to non-specific surface interactions. At higher concentrations, both isotherms approached saturation, indicating limited available adsorption sites. The higher adsorption capacity of HC@Mn–MIP–TiO_2 confirms the effectiveness of molecular imprinting in generating selective recognition sites and enhancing adsorption performance toward enrofloxacin.

The adsorption behavior of enrofloxacin on HC@Mn–MIP–TiO_2 and HC@Mn–NIP–TiO_2 was analyzed using Freundlich, Langmuir, and Temkin isotherm models (Fig. 14–16). The Freundlich model indicated favorable adsorption ($n > 1$) for both materials, although deviations at higher concentrations suggest limitations in describing site saturation. The Temkin model also showed good correlation, indicating adsorbate–adsorbent interactions and a gradual decrease in adsorption energy with increasing surface coverage. Among the models, the Langmuir isotherm provided the best fit ($R^2 > 0.99$), confirming monolayer adsorption on a finite number of uniform sites. The higher adsorption capacity and steeper Langmuir slope for HC@Mn–MIP–TiO_2 compared to HC@Mn–NIP–TiO_2 further demonstrate the effectiveness of molecular imprinting in creating selective recognition sites for enrofloxacin.

Figure 13: Adsorption Isotherm of ENR on HC@Mn-MIP-TiO_2 and HC@Mn-NIP-TiO_2

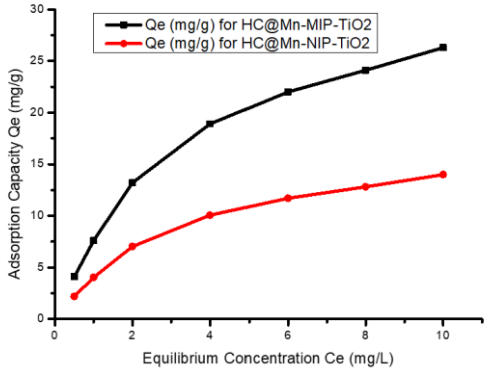

The equations for the respective isotherm models are given below.

Langmuir Isotherm	$\frac{C_e}{Q_e} = \frac{C_e}{Q_{max}} + \frac{1}{Q_{max}\, K_L}$
Freundlich Isotherm	$\ln Q_e = \ln K_F + \frac{1}{n} \ln C_e$
Temkin Isotherm	$Q_e = a + b \ln C_e$

4.4 Comparison between HC@Mn-MIP-TiO_2 and HC@Mn-NIP-TiO_2 Adsorbents (Imprinting Effect)

Langmuir adsorption parameters were obtained from linearized plots (C_e/Q_e vs. C_e), which showed good linearity for both HC@Mn–MIP–TiO_2 and HC@Mn–NIP–TiO_2, confirming the applicability of the Langmuir model (Figs. 15 and 17). The maximum adsorption capacity (Q_{max}) and Langmuir constant (K_L) were calculated from the slope and intercept of the fitted lines. HC@Mn–MIP–TiO_2 exhibited significantly higher Q_{max} and K_L values than HC@Mn–NIP–TiO_2, indicating the presence of more high-affinity binding sites generated by molecular imprinting. The imprinting factor derived from Langmuir capacities (IF_{linear} = 1.92) further confirms the enhanced adsorption performance of the imprinted material. These results indicate that enrofloxacin adsorption on HC@Mn–MIP–TiO_2 mainly occurs through monolayer coverage on energetically favorable recognition sites, whereas HC@Mn–NIP–TiO_2 exhibits weaker, non-specific adsorption. The enhanced adsorption of the MIP material is attributed to imprint-generated cavities complementary to enrofloxacin in size, shape, and functional group orientation, which also promote effective pre-concentration of the pollutant at the catalyst surface and facilitate subsequent photocatalytic degradation.

4.5 Selectivity Studies

The molecular recognition ability of HC@Mn–MIP–TiO_2 arises from specific interactions between the imprinted cavities and the target molecule, enrofloxacin (ENR). To evaluate selectivity and distinguish specific from nonspecific adsorption, competitive adsorption experiments were performed using ciprofloxacin (CIP) as a structural analogue. ENR and CIP share similar fluoroquinolone structures but differ in substituent orientation and steric configuration.

Figure 14: Freundlich Isotherms of HC@Mn-MIP-TiO_2 (Left) and HC@Mn-NIP-TiO_2 (Right)

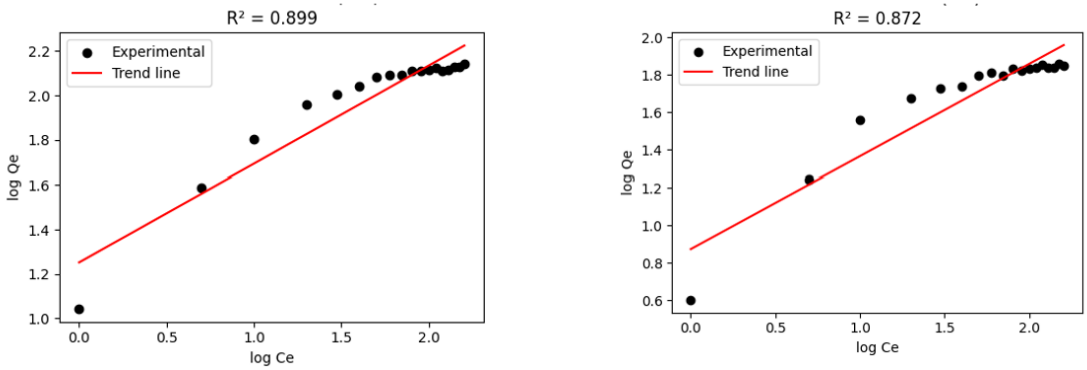

Figure 15: Langmuir Isotherms of HC@Mn-MIP-TiO_2 (Left) and HC@Mn-NIP-TiO_2 (Right)

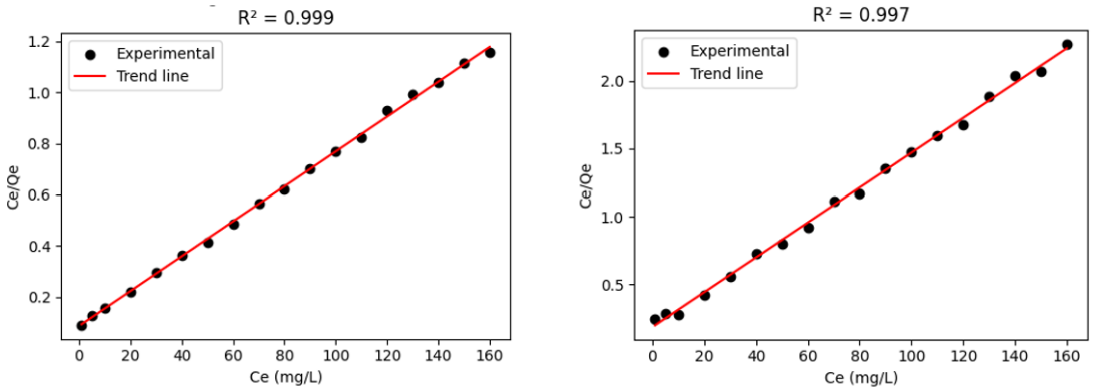

Figure 16: Temkin Isotherms of HC@Mn-MIP-TiO_2 (Left) and HC@Mn-NIP-TiO_2 (Right)

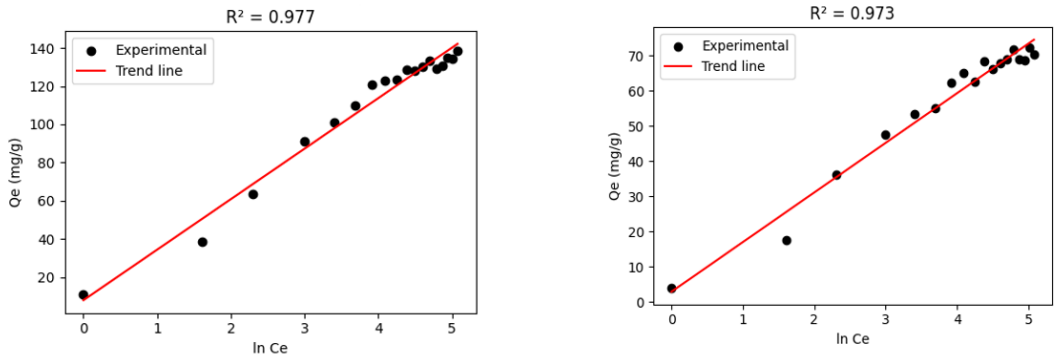

Batch adsorption experiments were conducted under identical conditions using equimolar solutions of ENR and CIP. The adsorption capacities of HC@Mn–MIP–TiO_2 and the non-imprinted material (HC@Mn–NIP–TiO_2) for both analytes were measured at equilibrium, and the imprinting factor (IF) was calculated as the ratio of adsorption capacity on the MIP to that on the NIP.

Figure 17: Langmuir fits for HC@Mn-MIP-TiO_2 and HC@Mn-NIP-TiO_2

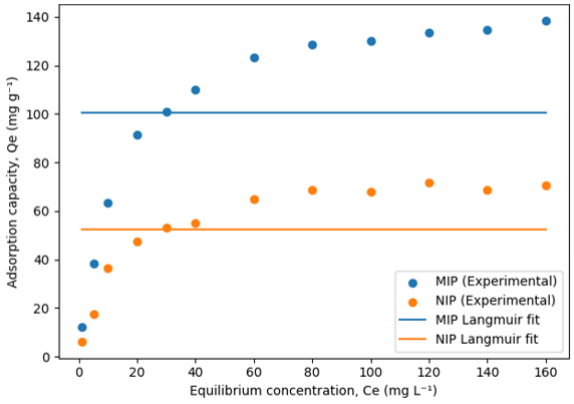

Table 2: Isotherm parameters for adsorption of ENR by HC@Mn-MIP-TiO_2 and HC@Mn-NIP-TiO_2

Adsorbent	Langmuir				Freundlich		Temkin		
	Q_{max} (mg g^{-1})	K_L (L mg^{-1})	R^2	KF	n	R^2	a	b	R^2
HC@Mn-MIP-TiO_2	149.2	0.071	0.999	38.6	1.41	0.899	11.8	27.4	0.977
HC@Mn-NIP-TiO_2	78.5	0.037	0.997	19.9	1.68	0.872	4.9	14.6	0.973

The selectivity coefficient (α) was calculated as $\alpha = IF_{ENR} / IF_{CIP}$. As shown in Table 2, the higher adsorption capacity, imprinting factor, and distribution coefficient for enrofloxacin compared with ciprofloxacin confirm the formation of selective recognition sites in the HC@Mn–MIP–TiO_2 matrix. The selectivity coefficient (α = 2.38) indicates significantly stronger affinity of the imprinted material toward the template molecule than its structural analogue, validating the molecular imprinting effect (Table 3).

Table 3: Selectivity Experiment Results

Analyte	Q_{MIP} (mg g^{-1})	Q_{NIP} (mg g^{-1})	IF (a)	K_d(MIP) (L g^{-1})	K_d (NIP) (L g^{-1})	α
ENR	149.2	78.1	1.91	14.84	7.85	2.38
CIP	92.6	63.5	1.46	9.26	6.35	—

Overall, the enhanced adsorption capacity and binding affinity of HC@Mn–MIP–TiO_2 toward enrofloxacin demonstrate effective molecular recognition arising from imprint-generated cavities.

5. Photocatalytic degradation of enrofloxacin

Photodegradation experiments of enrofloxacin were conducted for both Mn-doped molecularly imprinted titania (MIP) and the corresponding non-imprinted material (NIP) under identical conditions (Fig. 18 and 19).

Figure 18: Time-dependent UV–Vis spectra demonstrating the photocatalytic degradation of enrofloxacin by HC@Mn-MIP-TiO_2

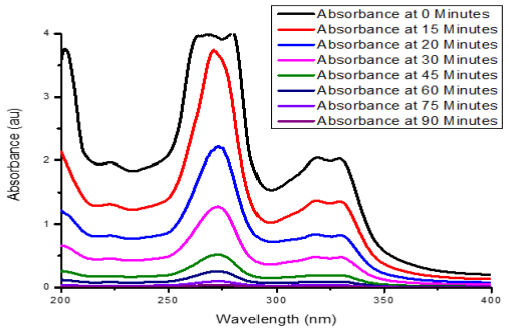

The concentration–time profiles monitored at ~270 nm showed a rapid decrease in enrofloxacin concentration in both systems. At an initial concentration of 10 ppm , HC@Mn–MIP–TiO_2 achieved 99.90% degradation within 90 min, while HC@Mn–NIP–TiO_2 reached 90.96%. Because degradation efficiencies near 100% may fall within experimental uncertainty, kinetic analysis provides a more reliable comparison. The pseudo-first-order rate constant for HC@Mn–MIP–TiO_2 (k_1 = 0.08297 min^{-1}) was higher than that of HC@Mn–NIP–TiO_2 (k_1 = 0.05756 min^{-1}), indicating faster degradation of enrofloxacin with the imprinted photocatalyst.

Figure 19: UV–Vis spectra showing time-dependent degradation of enrofloxacin by HC@Mn-NIP-TiO_2

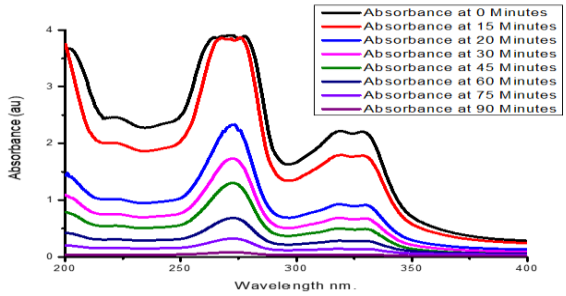

This enhanced performance is attributed to the presence of molecularly selective binding cavities in the HC@Mn–MIP–TiO_2 matrix, which facilitate stronger adsorption and more efficient photocatalytic degradation of enrofloxacin compared to the non-imprinted material. Although both photocatalysts exhibit high degradation efficiency, the higher rate constant of HC@Mn–MIP–TiO_2 indicates faster pollutant removal. The improved activity arises from the synergistic effects of Mn doping (enhanced charge separation), molecular imprinting (selective adsorption), and hollow morphology (improved light utilization).

5.1 Photocatalytic Degradation Performance of Enrofloxacin

The photocatalytic degradation of enrofloxacin (ENR) was evaluated by monitoring UV–Vis absorbance, residual concentration (C_t), degradation efficiency, and reaction kinetics under visible-light irradiation (Fig. 20).

Figure 20: UV–Vis spectra showing time-dependent degradation of enrofloxacin under Visible Light

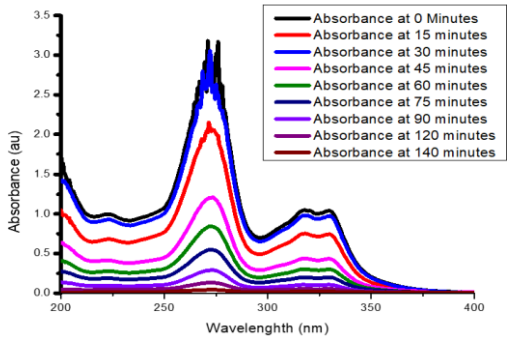

The initial ENR concentration (C_0) was 10 ppm. A rapid decrease in concentration was observed during the first 15 min (6.35 ppm), indicating fast photocatalytic activity. A temporary absorbance increase at 30 min (8.43 ppm) was attributed to intermediate species formed during degradation. Subsequently, ENR concentration decreased continuously to 3.73

ppm at 45 min and 0.90 ppm at 90 min, reaching near-complete degradation (0.13 ppm) after 140 min.

The degradation efficiency increased steadily from 36.50% at 15 min to 62.62% at 45 min and exceeded 80% by 75 min. Further irradiation resulted in efficiencies of 91.02% at 90 min, 95.90% at 120 min, and 98.72% after 140 min, indicating sustained photocatalytic activity without significant catalyst deactivation.

Kinetic analysis followed a pseudo-first-order model (Fig. 21). HC@Mn–MIP–TiO_2 exhibited the highest rate constant (k_1 = 0.08297 min^{-1}), compared with HC@Mn–NIP–TiO_2 (k_1 = 0.05756 min^{-1}) and the non-imprinted system (k_1 = 0.0323 min^{-1}). The higher rate constant of the imprinted photocatalyst demonstrates enhanced degradation kinetics due to selective adsorption and improved catalyst–pollutant interaction. Overall, the results confirm efficient visible-light photocatalytic degradation of ENR, with HC@Mn–MIP–TiO_2 showing superior performance.

Figure 21: Pseudo First Order Kinetics exhibited by Enrofloxacin

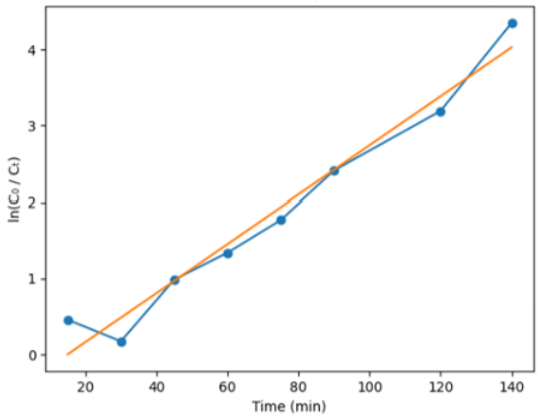

6. Recyclability and stability

The recyclability of HC@Mn–MIP–TiO_2 was evaluated to assess the reliability of the molecular imprinting process. Independent adsorption experiments were performed under identical conditions (initial ENR concentration, pH ~7.0, 25 ± 1 °C, adsorbent dose, and contact time) using separately prepared batches of the material. The equilibrium adsorption capacities showed minimal variation, with relative standard deviations below 5% (Fig. 22), indicating high reproducibility of the sol–gel imprinting and Mn-doping processes. In contrast, the non-imprinted material (HC@Mn–NIP–TiO_2) exhibited slightly greater variability due to the absence of specific recognition sites and reliance on nonspecific adsorption.

Figure 22: Reproducibility over Independent Batches

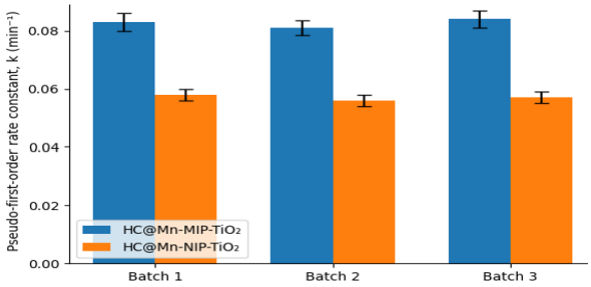

6.1 Regeneration and Reusability

The regeneration and reusability of HC@Mn–MIP–TiO_2 were evaluated through repeated adsorption–desorption cycles. After each adsorption experiment, the catalyst was recovered by centrifugation and desorbed using ethanol (or ethanol–water mixture) under stirring at room temperature. The regenerated material was washed with deionized water, dried at 40 °C, and reused under identical conditions. HC@Mn–MIP–TiO_2 retained ~85–90% of its initial adsorption capacity after five cycles, indicating good stability and reusability. The slight decline may be attributed to partial blockage of some imprinted cavities or minor material loss during handling (Fig. 23). In contrast, HC@Mn–NIP–TiO_2 showed a greater decrease in adsorption capacity upon reuse, reflecting weaker nonspecific interactions and lower structural stability without molecular imprinting.

Figure 23: Regeneration Performance Over Multiple Cycles

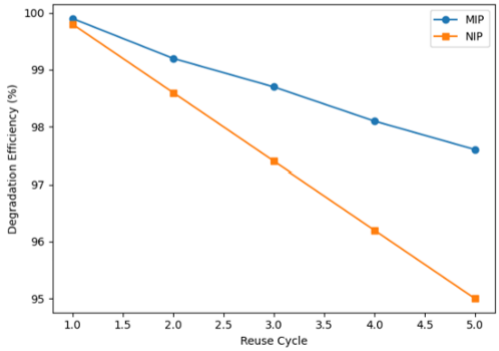

7. Application of HC@Mn–MIP–TiO_2 for Enrofloxacin Removal from Real Water Samples

The practical applicability of HC@Mn–MIP–TiO_2 was evaluated using spiked tap water and treated wastewater effluent. Samples were filtered through 0.45 μm membranes and used within 24 h. Each matrix was spiked with enrofloxacin (10 ppm) and photocatalytic experiments were performed under visible light using HC@Mn–MIP–TiO_2 (0.5 g L^{-1}) at natural pH after 30 min dark equilibration. ENR concentration was monitored by UV–Vis spectroscopy. Pseudo-first-order kinetics were observed in all matrices. The apparent rate

constants decreased from 0.08297 min^{-1} in ultrapure water to 0.04728 min^{-1} in tap water and 0.03907 min^{-1} in treated wastewater (Table 4).

Table 4: Photocatalytic degradation of ENR in real water samples

Water Matrix	k_1 (min^{-1})	R^2	Degradation at 90 min (%)	Degradation at 100 min (%)
Ultrapure water	0.08297	>0.99	99.9	~100
Tap water	0.04728	0.975	97.86	99.11
Treated wastewater	0.03907	0.948	97.93	98.55

Despite matrix interference, degradation efficiencies remained high (>97% within 100 min). The reduction in activity (pure water > tap water > wastewater) is attributed to competitive adsorption of dissolved organic matter, light attenuation, and radical scavenging by inorganic ions. The strong linearity (R^2 = 0.975 for tap water; 0.948 for wastewater) indicates that the photocatalytic mechanism remains unchanged in real matrices. The catalyst also demonstrated good stability in treated wastewater, retaining ~94% of its initial activity after five reuse cycles with only minor loss due to surface fouling (Fig. 24).

Figure 24: Reusability Studies

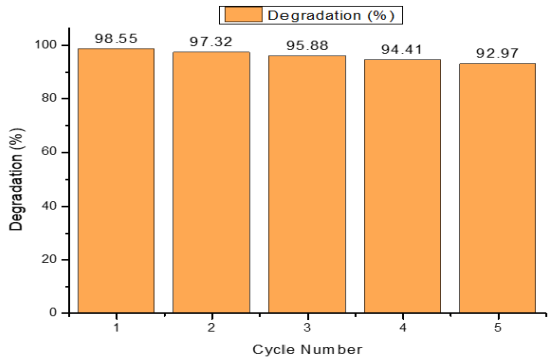

These results confirm that the synergistic effects of Mn doping, molecular imprinting, and hollow architecture enable efficient visible-light degradation of enrofloxacin even in complex water matrices, highlighting the potential of HC@Mn–MIP–TiO_2 for practical antibiotic removal in wastewater treatment.

8. Conclusions

XRD analysis confirmed that HC@Mn–MIP–TiO_2 maintains a phase-pure anatase TiO_2 structure after Mn doping, molecular imprinting, alkaline etching, and calcination, with no detectable manganese oxide phases. UV–Vis diffuse reflectance spectroscopy showed a red shift with band-gap narrowing to ~2.78 eV, enabling visible-light activation. FTIR analysis

verified successful removal of the enrofloxacin template and the presence of hydroxyl-rich surfaces favorable for adsorption and photocatalysis. Adsorption studies revealed a clear imprinting effect, with HC@Mn–MIP–TiO_2 showing higher adsorption capacity and selectivity (~2.4) toward enrofloxacin over ciprofloxacin. Photocatalytic experiments demonstrated faster degradation kinetics for the imprinted catalyst under visible light. The enhanced performance arises from the synergistic effects of Mn doping, molecular imprinting, and hollow morphology. Recyclability tests confirmed stable performance over multiple cycles, indicating good structural and functional stability. Overall, Mn-doped molecularly imprinted hollow TiO_2 nanospheres represent an efficient and selective photocatalyst for targeted removal of antibiotic contaminants from water.

Acknowledgements
The authors sincerely acknowledge the Department of Chemistry, Mata Gujri College, Fatehgarh Sahib, for providing the necessary laboratory infrastructure and instrumental facilities to carry out this work.

Declarations:

Consent to Participate: All authors have agreed to participate in the preparation and revision of the manuscript.

Consent to Publish: All authors have approved the submission and publication of this manuscript.

Competing Interests: The authors declare that they have no competing interests.

References:

[1] P. Vikesland, E. Garner, S. Gupta, S. Kang, A. Maile-Moskowitz, N. Zhu, Differential Drivers of Antimicrobial Resistance across the World, Acc. Chem. Res., 52 (2019) 916–924.
[2] O.P. Bansal, Antibiotics in hospital effluents and their impact on the antibiotics resistant bacteria and remediation of the antibiotics: a review, Netw. Pharmacol., 4 (2019) 6–30.
[3] S.A. Kraemer, A. Ramachandran, G.G. Perron, Antibiotic pollution in the environment: from microbial ecology to public policy, Microorganisms, 7 (2019) 180.
[4] I. Tbessi, M. Benito, E. Molins, J. LIorca, A. Touati, S. Sayadi, W. Najjar, Effect of Ce and Mn co-doping on photocatalytic performance of sol-gel TiO_2, Solid State Sci., 88 (2019) 20–28.
[5] X.H. Xia, L. Lu, A.S. Walton, M. Ward, X.P. Han, R. Brydson, J.K. Luo, G. Shao, Origin of significant visible-light absorption properties of Mn-doped TiO_2 thin films, Acta Mater., 60 (2012) 1974–1985.
[6] B. Choudhury, A. Choudhury, Tailoring luminescence properties of TiO_2 nanoparticles by Mn doping, J. Lumin., 136 (2013) 339–346.

[7] M.S. Mahmoud, E. Ahmed, A.A. Farghali, A.H. Zaki, E.A. Abdelghani, N.A. Barakat, Influence of Mn, Cu, and Cd–doping for titanium oxide nanotubes on the photocatalytic activity toward water splitting under visible light irradiation, Colloids Surf. Physicochem. Eng. Asp., 554 (2018) 100–109.

[8] D. Zhang, F. Zeng, Characterization, activity and mechanisms of a visible light driven photocatalyst: Manganese and iron co-modified TiO_2 nanoparticles, Russ. J. Phys. Chem. A, 85 (2011) 1825–1831.

[9] V.D. Binas, K. Sambani, T. Maggos, A. Katsanaki, G. Kiriakidis, Synthesis and photocatalytic activity of Mn-doped TiO_2 nanostructured powders under UV and visible light, Appl. Catal. B Environ., 113 (2012) 79–86.

[10] R. Chauhan, A. Kumar, R.P. Chaudhary, Structural and photocatalytic studies of Mn doped TiO_2 nanoparticles, Spectrochim. Acta. A. Mol. Biomol. Spectrosc., 98 (2012) 256–264.

[11] X. Liu, P. Lv, G. Yao, C. Ma, P. Huo, Y. Yan, Microwave-assisted synthesis of selective degradation photocatalyst by surface molecular imprinting method for the degradation of tetracycline onto $ClTiO_2$, Chem. Eng. J., 217 (2013) 398–406.

[12] X. Shen, L. Zhu, C. Huang, H. Tang, Z. Yu, F. Deng, Inorganic molecular imprinted titanium dioxide photocatalyst: synthesis, characterization and its application for efficient and selective degradation of phthalate esters, J. Mater. Chem., 19 (2009) 4843–4851.

[13] X. Shen, L. Zhu, G. Liu, H. Yu, H. Tang, Enhanced Photocatalytic Degradation and Selective Removal of Nitrophenols by Using Surface Molecular Imprinted Titania, Environ. Sci. Technol., 42 (2008) 1687–1692.

[14] M. Cantarella, S.C. Carroccio, S. Dattilo, R. Avolio, R. Castaldo, C. Puglisi, V. Privitera, Molecularly imprinted polymer for selective adsorption of diclofenac from contaminated water, Chem. Eng. J., 367 (2019) 180–188.

[15] X. Shen, L. Zhu, N. Wang, L. Ye, H. Tang, Molecular imprinting for removing highly toxic organic pollutants, Chem. Commun., 48 (2012) 788–798.

[16] L. Chen, X. Wang, W. Lu, X. Wu, J. Li, Molecular imprinting: perspectives and applications, Chem. Soc. Rev., 45 (2016) 2137–2211.

[17] G. Prieto, H. Tüysüz, N. Duyckaerts, J. Knossalla, G.-H. Wang, F. Schüth, Hollow Nano- and Microstructures as Catalysts, Chem. Rev., 116 (2016) 14056–14119.

[18] M. Xiao, Z. Wang, M. Lyu, B. Luo, S. Wang, G. Liu, H. Cheng, L. Wang, Hollow Nanostructures for Photocatalysis: Advantages and Challenges, Adv. Mater., 31 (2019) 1801369.

[19] W.J. Tseng, P.-S. Chao, Synthesis and photocatalysis of TiO_2 hollow spheres by a facile template-implantation route, Ceram. Int., 39 (2013) 3779–3787.

[20] X. Wang, J. Feng, Y. Bai, Q. Zhang, Y. Yin, Synthesis, Properties, and Applications of Hollow Micro-/Nanostructures, Chem. Rev., 116 (2016) 10983–11060.